GPS Solutions (2025) 29:186
https://doi.org/10.1007/s10291-025-01946-1

RESEARCH PAPER

Multi-constellation instantaneous single difference triple-carrier ambiguity resolution in urban environments

Qi Cheng[1] · Wu Chen[1] · Junhui Wang[1] · Xiaolong Mi[1] · Yang Yang[1] · Rui Sun[2]

Received: 27 February 2025 / Accepted: 5 August 2025 / Published online: 13 August 2025

Abstract

The demand for high-precision real-time positioning is critical for applications such as autonomous vehicles, urban planning, and location-based services. Real-time kinematic (RTK) can provide centimeter-level positioning services and is widely used. However, the traditional intra-system double-difference model in RTK requires sacrificing one reference satellite per constellation, leading to insufficient satellite pairs for ambiguity resolution in challenging environments. To address this issue, we propose a single-difference triple-carrier ambiguity resolution (TCAR) algorithm. This algorithm estimates relative measurement biases in advance, and these biases require re-estimation whenever the receiver is replaced or restarted. These estiamted biases are then used to correct real-time GNSS measurements, enabling instantaneous single-difference TCAR. Random sampling consensus (RANSAC) is employed to detect and exclude satellites with incorrectly fixed ambiguities before positioning. To validate the effectiveness of the proposed algorithm, both static and vehicular experiments were conducted in challenging urban environments. In the static experiment, the results demonstrate that the positional availability of the proposed algorithm (92.1%) is significantly higher than that of the two comparative algorithms, which achieved 68.3% and 54.5%, respectively. The positioning accuracies of the three algorithms are comparable, with 3D Root Mean Square Errors (RMSEs) of 5.03 cm, 4.41 cm, and 5.43 cm. In the vehicular experiment, the proposed algorithm achieved nearly 100% positional availability in typical urban areas, with an RMSE of 5.28 cm, outperforming the two comparative algorithms, with availabilities of 94.7% and 78.2%, and 3D RMSEs of 6.33 cm and 3.64 cm. These results highlight the ability of the proposed algorithm to provide continuous, reliable and precise real-time positioning in challenging urban environments.

Keywords GNSS · TCAR · FDE · Single-difference · Measurement bias · Urban environments

Introduction

The rapid global urbanization has significantly increased the demand for precise geospatial data, thereby necessitating advancements in positioning technologies. Real-Time Kinematic (RTK) positioning has emerged as a crucial technology in this field, offering the potential for centimeter-level accuracy that is essential for numerous urban applications (Li et al. 2021a, b, 2023), such as intelligent transportation systems. RTK employs differential correction techniques to mitigate the majority of systematic errors in Global Navigation Satellite Systems (GNSS) measurements, facilitating the resolution of integer ambiguity (Ng and Hsu 2021; Cheng at al. 2023). Integer ambiguity refers to the exact number of full wavelengths of the carrier signal, which must be accurately resolved to achieve high-precision positioning. However, resolving integer ambiguities

✉ Rui Sun
rui.sun@nuaa.edu.cn

Qi Cheng
qi001.cheng@connect.polyu.hk

Wu Chen
wu.chen@polyu.edu.hk

Junhui Wang
junhui01.wang@connect.polyu.hk

Xiaolong Mi
xiaolong.mi@polyu.edu.hk

Yang Yang
yyoung.yang@polyu.edu.hk

[1] Department of Land Surveying and Geo-Informatics, The Hong Kong Polytechnic University, Kowloon, Hong Kong

[2] College of Civil Aviation, Nanjing University of Aeronautics and Astronautics, Nanjing 211106, China

becomes challenging in urban environments due to dense infrastructure that can interfere with GNSS signal reception. The adverse effects on GNSS signals in urban areas can be categorized as follows: (1) increased errors resulting from multipath effects, Non-Line-Of-Sight (NLOS) conditions, and electromagnetic interference, and (2) a reduced number of visible satellites due to signal obstruction and attenuation.

Recently, many techniques have been used to mitigate the larger errors of GNSS measurements for high-precision positioning. These strategies mainly focus on three different types for the NLOS/multipath mitigation. The first type is based on the special designed antenna, such as chock-ring antenna (Tranquilla et al. 1994), dual-polarisation antenna (Jiang and Groves 2014; Sun et al. 2021), and antenna array (Daneshmand et al. 2013; Vagle et al. 2016). The second type is based on the signal processing in a receiver, for example, narrow corrector (Van Dierendonck et al. 1992) and multipath estimating delay lock loop (Van Nee et al. 1994). The last type is based on the evaluation of GNSS raw observations, such as carrier-to-noise ratio (C/N0) (Groves and Jiang 2013) and elevation angle (Heng et al. 2014; Dyukov 2016; Malicorne et al. 2002). Consistency check among GNSS measurements can also be used for the fault detection and exclusion (FDE) of satellites (Groves and Jiang 2013).

In our previous work, we demonstrated that consistency check using GNSS three-frequency measurements hold significant promise for enhancing the availability of high-precision positioning services in urban environments (Cheng et al. 2024). In that approach, ambiguities are initially resolved using a Triple-Carrier Ambiguity Resolution (TCAR) method, followed by detection and selection through tailored RANdom SAmple Consensus (RANSAC). This process markedly improves positional availability compared to traditional methods, without compromising positioning accuracy. This advantage arises from the use of a geometry-free model, where integer ambiguities are determined solely by the observations of the corresponding satellite-pair. Consequently, large errors in the measurements from satellite A (non-reference satellite) do not affect the ambiguity resolution for satellite B, a limitation inherent in geometry-based models. While excluding satellites with incorrectly fixed ambiguities can maintain positioning accuracy, it exacerbates the issue of insufficient satellites, thereby constraining further improvements in positional availability.

Utilizing multiple satellite constellations is an effective strategy to increase the number of available satellites for positioning. However, in the traditional intra-system double-difference model, also known as loose integration, this advantage is diminished because each constellation requires a reference satellite (Yang et al. 2020; Geng et al. 2019). These reference satellites are essentially sacrificed to eliminate common errors, such as receiver clock offsets and hardware delays. Since current receivers can only ensure that these common errors are consistent within the same measurement, for example GPS L1 pseudorange, the intra-system double-difference model is widely employed. To address this limitation, numerous researchers have investigated the stability of biases across different measurements, especially measurements from different systems (Odijk et al. 2012; Odijk and Teunissen 2013; Paziewski and Wielgosz 2015; Paziewski et al. 2015; Li et al. 2018; Gao et al. 2018). Their findings indicate that the measurement biases of certain receivers are stable and can be considered constant over short time periods, such as a single day. Building on this insight, an inter-system double-difference model, also known as tight integration, has been investigated, using overlapping frequencies (Chen et al. 2022). For instance, GPS L1, QZSS L1, Galileo E1, and BDS3 B1C share the same frequency of 1575.42 MHz. In this new model, biases are first estimated and corrected, after which a single reference satellite is selected for all satellites across different constellations. This approach significantly enhances the strength of model, particularly in urban environments (Chen et al. 2019; Li et al. 2021a, b).

However, the limited frequency overlap among different satellite systems restricts the use of this model. Consequently, there has been increased focus on the tight integration of non-overlapping frequencies (Zhao et al. 2023). Due to the different wavelengths of these non-overlapping frequencies, the inter-system double-difference ambiguity is not an integer. Strategies have been developed to address this issue (Gao et al. 2018; Zhao et al. 2023). A critical factor is the single-difference ambiguity of the selected reference satellite. If the ambiguity is unknown, the strength of the inter-system model will be weakened. The single-difference ambiguity of the reference satellite is typically absorbed into the estimated biases (Gao et al. 2021; Zhao et al. 2023). This implies that when cycle slips occur or the reference satellite changes, the estimated biases between different measurements should be re-estimated, or a new ambiguity of the reference satellite needs to be resolved (Gao et al. 2021; Shang et al. 2020). The complexity of urban environments may negatively impact the performance of inter-system double-difference model, particularly for single-epoch positioning. In fact, the model strength of inter-system is enhanced by reducing the numbers of receiver clock errors. In the inter-system double-difference model, the receiver clock errors of different systems are equal after bias calibration. Nevertheless, the pseudorange-carrier and multi-frequency (within a constellation) biases are ignored in the inter-system double-difference model. This means that the model strength can be further enhanced using the between-receiver single-difference model by calibrating the pseudorange-carrier and multi-frequency (within a constellation) biases. Recently,

most related research has focused on geometry-based ambiguity resolution (Mi et al. 2021; Shang et al. 2020). The single-difference geometry-free model for ambiguity resolution warrants more attentions, especially as more frequencies become available across different constellations.

In this paper, we propose an instantaneous RANSAC-based single-difference TCAR algorithm. The initial step of this algorithm involves estimating the biases present among different measurements. These biases should be corrected before resolving ambiguities. The primary objectives of this correction process are twofold: first, to ensure that the single-difference receiver clock errors of all measurements, including pseudorange and carrier phase of different constellations (frequencies), are consistent, and second, to preserve the integer nature of all carrier phase ambiguities. Following these preparatory steps, the TCAR can be applied to resolve the ambiguities for single-difference measurements of each satellite. The RANSAC algorithm is employed to detect and exclude satellites with incorrectly resolved ambiguities before proceeding with positioning. The proposed algorithm can work in real-time, which can provide positioning services in challenging urban environments.

Methodology

The framework of the proposed RANSAC-based single-difference TCAR is illustrated in Fig. 1. In this algorithm, measurement biases are estimated during the initialization phase. Then, these estimated biases are used to correct the received single-difference measurements in real-time. Following these corrections, the single-difference ambiguity of the extra-wide-lane (EWL) is initially resolved using pseudoranges. Subsequently, the ambiguities of the wide-lane (WL) and original frequencies are resolved sequentially. Once the original ambiguities of all observed satellites are fixed, the RANSAC algorithm is used to exclude satellites with incorrectly fixed ambiguities (outliers). If the number of remaining satellites (inliers) exceeds a threshold (explain later), the positioning process proceeds. Otherwise, high-precision positioning cannot be achieved at this epoch. Further details are provided in the subsequent sections.

Bias Estimation

Since only a short baseline is considered in this paper, most systematic errors, such as satellite orbit and clock errors, as well as atmospheric errors, including ionospheric and tropospheric delays, can be effectively mitigated and ignored through the between-receiver single-difference techniques. The single-difference pseudorange and carrier phase measurements can be mathematically represented as follows:

$$P_i^A = \rho^A + c\,dt_r + BIAS_{P_i}^A + \varepsilon_i^A \tag{1}$$

$$L_i^A = \rho^A + c\,dt_r + BIAS_{L_i}^A + \lambda_i^A N_i^A + \epsilon_i^A \tag{2}$$

where, the single-difference operator Δ is omitted for brevity; A denotes the constellation, and i signifies the frequency; The symbols P and L represent the pseudorange and carrier phase, respectively; The term ρ refers to the geometric range after single-difference; The constant c represents

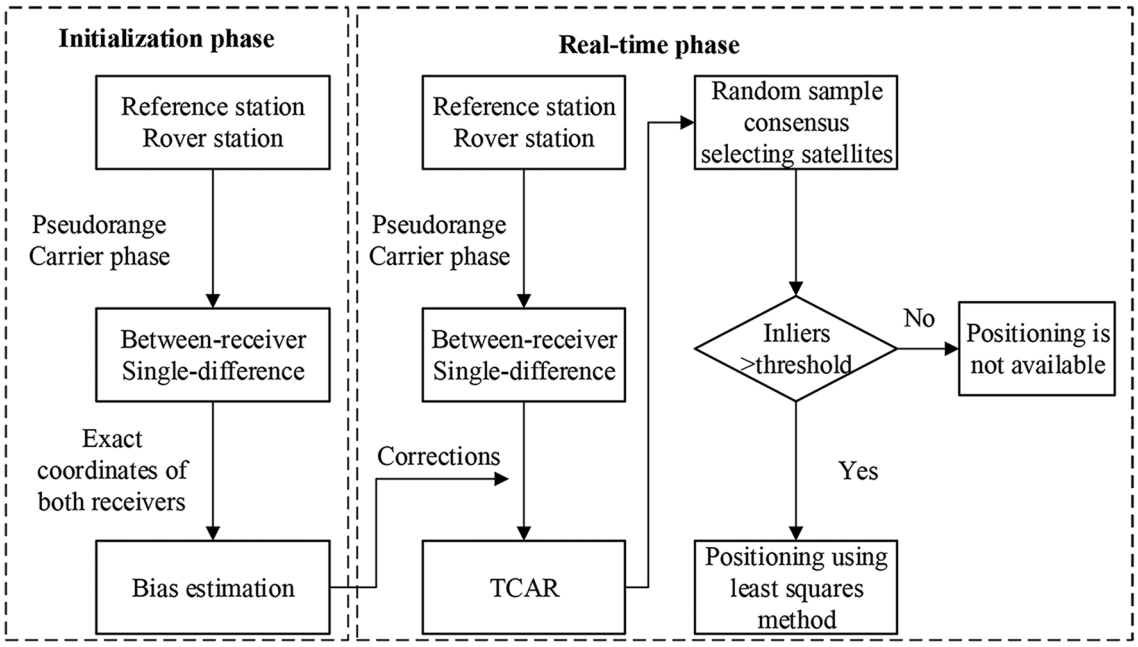

Fig. 1 Framework of the proposed single-difference triple-carrier ambiguity resolution

the speed of light in a vacuum; λ denotes the wavelength of carrier phase, and N represents the integer ambiguity; ϵ and ϵ correspond to the random noise components of the pseudorange and carrier phase, respectively; dt_r indicates the single-difference receiver clock offset; *BIAS* primarily arises from hardware delays, which may not be equal for different measurements.

In traditional algorithms, these hardware delays are combined with the receiver clock offset to form mixed receiver clock errors. This is the reason why the receiver clock errors of different frequencies and constellations are estimated separately, since they are not equal. Isolating the absolute *BIAS* from the receiver clock error proves to be challenging and, in practice, unnecessary (Mi et al. 2021). We only need to estimate and correct the relative measurement biases to guarantee that (1) the single-difference receiver mixed clock errors of all measurements, including pseudorange and carrier phase of different constellations (frequencies), are consistent, and (2) the integer nature of all carrier phase ambiguities. To estimate these biases, present in different measurements, one type of measurement should be selected as the benchmark. The relative biases of other measurements with respect to this benchmark must be estimated and subsequently applied for correction. It is essential that the benchmark measurement be the carrier phase in order to preserve the integer nature of the ambiguity. Assuming that GPS L1 carrier is chosen as the benchmark, the equation can be reorganized as follows:

$$L_1^G = \rho^G + c\,\tilde{dt}_r + \epsilon_1^G \tag{3}$$

where, $\tilde{dt}_r$ is the new mixed receiver error, with $c\,\tilde{dt}_r = c\,dt_r + BIAS_{L_1}^G + \lambda_1^G N_1^G$. Other measurements can be rewritten as:

$$P_i^A = \rho^A + c\tilde{dt}_r + BIAS_{P_i}^A - BIAS_{L_1}^G - \lambda_1^G N_1^G + \varepsilon_i^A \tag{4}$$

$$L_i^A = \rho^A + c\tilde{dt}_r + BIAS_{L_i}^A + \lambda_i^A N_i^A - BIAS_{L_1}^G - \lambda_1^G N_1^G + \epsilon_i^A \tag{5}$$

The corresponding relative biases for P_i^A and L_i^A are $BIAS_{P_i}^A - BIAS_{L_1}^G - \lambda_1^G N_1^G$ and $BIAS_{L_i}^A + \lambda_i^A N_i^A - BIAS_{L_1}^G - \lambda_1^G N_1^G$, respectively. They can be obtained by subtracting Eq. (3) from Eqs. (4) and (5), respectively.

$$\begin{aligned} &BIAS_{P_i}^A - BIAS_1^G - \lambda_1^G N_1^G \\ &= (P_i^A - L_1^G) - (\rho^A - \rho^G) - (\varepsilon_i^A - \varepsilon_1^G) \end{aligned} \tag{6}$$

$$\begin{aligned} &BIAS_{L_i}^A + \lambda_i^A N_i^A - BIAS_{L_1}^G - \lambda_1^G N_1^G \\ &= \left(L_i^A - L_1^G\right) - \left(\rho^A - \rho^G\right) - (\in_i^A - \in_1^G) \end{aligned} \tag{7}$$

For measurements from the same constellation, the geometric range difference $\left(\rho^A - \rho^G\right)$ can be ignored due to the identical signal propagation path. For measurements from different constellations, if the precise coordinates of both receivers are known, the geometric range difference $\left(\rho^A - \rho^G\right)$ can be calculated and subsequently removed. Even though obtaining precise coordinates for the reference station is not difficult, determining them for the rover station presents a challenge. In this case, the coordinates of the rover station can be estimated using the traditional intra-system double-difference algorithm in relative open areas. As a result, the relative biases estimation can be transformed into:

$$BIAS_{P_i}^A - BIAS_{L_1}^G - \lambda_1^G N_1^G = (P_i^A - L_1^G) - (\varepsilon_i^A - {}_1^G) \tag{8}$$

$$BIAS_{L_i}^A + \lambda_i^A N_i^A - BIAS_{L_1}^G - \lambda_1^G N_1^G = \left(L_i^A - L_1^G\right) - (\epsilon_i^A - \epsilon_1^G) \tag{9}$$

Here, the designed relative measurement biases can be estimated within a single-epoch, if the precisie position of rover station is known. To enhance accuracy, the average value over a time series can be employed to smooth the noise present in the pseudorange and carrier phase measurements. It worth noting that cycle slips should be detected and repaired during this smoothing process. The estimated relative biases can then be applied to correct the single-difference measurements before the TCAR. It should be noted that an important limitation is that, for the majority of current receivers, these biases are only valid before a receiver restart. Consequently, when the receiver is replaced or restarted, re-estimation of these biases becomes necessary.

Bias correction and single-difference TCAR

Once the relative biases for each single-difference measurement have been obtained, all subsequent measurements can be corrected, as these biases tend to remain relatively stable over time. Using GPS as an example, frequencies 1, 2, and 3 correspond to L1, L2, and L5. the corrected single-difference three-frequency measurements are as follows:

$$\begin{cases} L_1^G = r + \lambda_1^G N_1^G + \epsilon_1^G \\ \tilde{L_2^G} = r + \lambda_2^G N_2^G + \epsilon_2^G \\ \tilde{L_3^G} = r + \lambda_3^G N_3^G + \epsilon_3^G \\ \tilde{P_1^G} = r + \epsilon_1^G \\ \tilde{P_2^G} = r + \epsilon_2^G \\ \tilde{P_3^G} = r + \epsilon_3^G \end{cases} \tag{10}$$

with $r = \rho^G + c\tilde{dt}_r$; Here, these pseudorange and carrier phase measurements have been corrected by the estimated

biases in the previous section. The N_1^G, N_2^G and N_3^G are integer ambiguity and unknown. It is important to note that in Eqs. (3) and (5) the integer ambiguities are absorbed by receiver clock error and biases. If no cycle slip occurs, the corrected carrier phase actually has no ambiguity, or in other words, the ambiguity is zero. However, this is true only for the satellites involved in the bias calculation, the satellite of each constellation with highest elevation angle in this paper; it does not apply to the satellites that are not involved. Due to the frequent cycle slip in the real-time, the ambiguities of all satellites are consider unknown, and needed to be resolved instantaneously. The average r, i.e. r_1, can be expressed as:

$$r_1 = \frac{\tilde{P_1^G} + \tilde{P_2^G} + \tilde{P_3^G}}{3} \tag{11}$$

The ambiguity of extra-wide-lane ($N_{(0,\,1,\,-1)}$) can be calculated as:

$$N_{(0,\,1,\,-1)} = round\,((\frac{\tilde{L_2^G}}{\lambda_2^G} - \frac{\tilde{L_3^G}}{\lambda_3^G}) - (\frac{r_1}{\lambda_2^G} - \frac{r_1}{\lambda_3^G})) \tag{12}$$

where, $round\,()$ refers to the rounding function that rounds a number to the nearest integer. After the fixing of the $N_{(0\,1\,-1)}$, the value of a more accurate r, r_2, can be updated as:

$$r_2 = \lambda_{\,(0,1,-1)} \times \ (l_{(0,1,-1)} - N_{(0,1,-1)}) \tag{13}$$

with $\lambda_{\,(0,1,-1)} = \frac{1}{\lambda_2^G} - \frac{1}{\lambda_3^G}$, and $l_{(0,1,-1)} = \frac{\tilde{L_2^G}}{\lambda_2^G} - \frac{\tilde{L_3^G}}{\lambda_3^G}$. Then the ambiguity of wide-lane ($N_{(1,-1,\,0)}$) can be fixed with the aid of r_2

$$N_{(1,-1,\,0)} = round\,((\frac{\tilde{L_1^G}}{\lambda_1^G} - \frac{\tilde{L_2^G}}{\lambda_2^G}) - (\frac{r_2}{\lambda_1^G} - \frac{r_2}{\lambda_2^G})) \tag{14}$$

With the fixed $N_{(0,\,1,\,-1)}$ and $N_{(1,-1,\,0)}$, equations can be summaried as:

$$\begin{cases} N_{(1,-1,0)} = N_1^G - N_2^G \\ N_{(0,1,-1)} = N_2^G - N_3^G \\ \tilde{L_1^G} = r + \lambda_1^G N_1^G + \epsilon_1^G \\ \tilde{L_2^G} = r + \lambda_2^G N_2^G + \epsilon_2^G \\ \tilde{L_3^G} = r + \lambda_3^G N_3^G + \epsilon_3^G \end{cases} \tag{15}$$

Here, we have five equations and four unknows, and these ambiguities are integer. The integer least-suqares can be used to compute the final solution $(\tilde{r},\, N_1^G,\, N_2^G,\, N_3^G)$. When there *n* satellites whose ambiguities are fixed, we have:

$$\begin{bmatrix} I_1 & 1 \\ I_2 & 1 \\ \vdots & \\ I_n & 1 \end{bmatrix}_{n\times 4} \cdot\ \Delta X = \begin{bmatrix} \tilde{r}^1 \\ \tilde{r}^2 \\ \vdots \\ \tilde{r}^n \end{bmatrix}_{n\times 1} \tag{16}$$

where, I_i is the unit vector pointing from the approximate position of the rover station to *i-th* satellite. The term $\Delta X = (\Delta x, \Delta y, \Delta z, \tilde{cdt_r})$, which includes the positional correction and the mixed receiver clock error, can be calculated using the least squares method. $\tilde{r}^i$ is obtained from Eq. (15) using three-frequency measurements of *i-th* satellite. The satellites in Eq. (16) may belong to different constellations, but only with one common receiver clock error. This can enhance the strength of the positioning model for multi-constellation, which is important in a challenging environment.

Random sample consensus (RANSAC) based satellite selection

It is not feasible to correctly resolve ambiguities for all satellites within a single-epoch. To ensure high-precision positioning, it is essential to identify and exclude incorrect ambiguities before the positioning process. The RANSAC algorithm can be employed to effectively accomplish this task (Cheng et al. 2024). RANSAC is an iterative method used for estimating the parameters of a mathematical model from a set of observed data that contains outliers. This algorithm operates by repeatedly selecting a random subset of the data points, fitting a model to this subset, and then determining how many data points from the entire set fit this model within a predefined tolerance (Fischler and Bolles 1981). The process is repeated until the stopping condition is met. The model with the highest consensus set, or the largest number of inliers, is considered the best estimate.

For brevity, let $G_{n\times 4} = \begin{bmatrix} I_1 & 1 \\ I_2 & 1 \\ \vdots & \\ I_n & 1 \end{bmatrix}_{n\times 4}$, $R_{n\times 1} = \begin{bmatrix} \tilde{r}^1 \\ \tilde{r}^2 \\ \vdots \\ \tilde{r}^n \end{bmatrix}_{n\times 1}$. In the RANSAC processing, subsets are generated by randomly selecting satellites. Each subset should include four satellites to account for the four unknowns in the system. When there are *n* satellites available from different constellations, the number of possible subsets that can be generated is given by:

$$C_n^4 = \frac{n \cdot (n-1) \cdot (n-2) \cdot (n-2)}{4 \cdot 3 \cdot 2 \cdot 1} \tag{17}$$

Each subset contains four satellites, and then the subset series are:

$$\{ (1,2,3,4) \quad (1,2,3,5) \quad \cdots \quad (n-3, n-2, n-1, n) \} \tag{18}$$

For a satellite subset (i, j, k, l), the corresponding equations from Eq. (16) are:

$$\begin{bmatrix} I_i & 1 \\ I_j & 1 \\ I_k & 1 \\ I_l & 1 \end{bmatrix}_{4\times 4} \cdot \Delta X = \begin{bmatrix} \tilde{r}^i \\ \tilde{r}^j \\ \tilde{r}^k \\ \tilde{r}^l \end{bmatrix}_{4\times 1} \tag{19}$$

Based on the least squares method, we have:

$$\Delta X_{(i,j,k,l)} = \left(G^T_{(i,j,k,l)} G_{(i,j,k,l)}\right)^{-1} G^T_{(i,j,k,l)} R_{(i,j,k,l)} \tag{20}$$

Then, substituting $\Delta X_{(i,j,k,l)}$ into Eq. (16) allows the residuals for all satellites to be obtained:

$$V_{n\times 1} = R_{n\times 1} - G_{n\times 4} \cdot \Delta X_{(i,j,k,l)} \tag{21}$$

where, $V_{n\times 1} = [v^1\ v^2\ \cdots\ v^n]^T$ represents the residual vector corresponding to all tracked satellites. If the absolute value of v^m is less than a specified threshold (5 cm in this paper), the *m-th* satellite can be considered an inlier. This process is repeated until all subsets have been evaluated. The inlier set containing the largest number of satellites will be selected as the final result, which needs to be validated by a predetermined threshold, since more inliers in the final set indicate a more robust solution. Five (four unknowns + one redundancy) and seven (four unknowns + three redundancies) are selected as the thresholds to determine accepting this solution or not for the static and vehicular experiments respectively in this paper. If the number of satellites in the final inlier set exceeds the threshold, the positioning corrections and mixed receiver clock error can be calculated as follows:

$$\Delta X_{inliers} = \left(G^T_{inliers} G_{inliers}\right)^{-1} G^T_{inliers} R_{inliers} \tag{22}$$

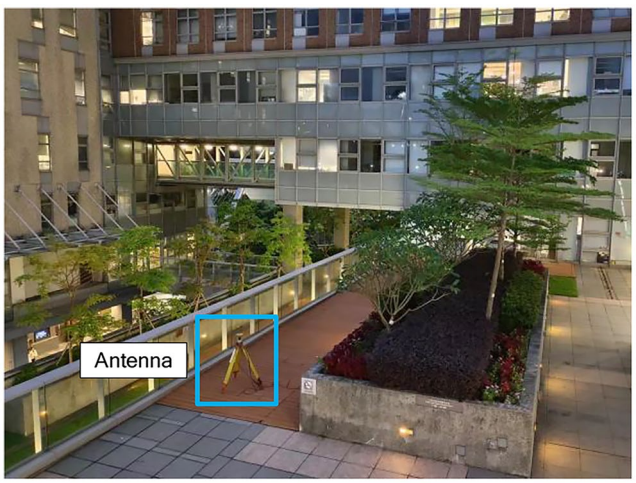

Fig. 2 Static experimental environment

Static experiment

The static experiment was conducted in a GNSS challenging environment in Hong Kong, as illustrated in Fig. 2. The receiver was surrounded by walls, resulting in severe NLOS/multipath signal interference. Three-frequency data from Galileo and BDS2 were collected. Figure 3 presents the visible satellites and their elevation angles for each constellation, with a cut-off angle of 10 degrees and a carrier-to-noise density ratio (C/N0) threshold of 35 dB-Hz. For BDS, four satellites were consistently tracked almost throughout the experimental period, whereas the number of Galileo satellites ranged from one to four. The elevation angles for BDS satellites were approximately between 40 and 90 degrees. In contrast, the elevation angles for Galileo satellites were lower, ranging from 10 to 80 degrees, suggesting that Galileo measurements might be more susceptible to severe NLOS/multipath interference. Detailed information about the experimental setup is provided in Table 1. The entire experiment lasted for one hour, with a sampling rate of 1 Hz. A short baseline of 3.9 km was employed, allowing atmospheric errors to be ignored in the subsequent ambiguity resolution processing steps. The linear combinations of the EWL and WL are also included in Table 1.

Bias Estimation

Before the ambiguity resolution, the relative measurement biases should be analysed and estimated for further correction. Given that there is no obvious bias among satellites within a single constellation for each frequency, we select the satellite with the highest elevation angle from each constellation for bias estimation. In this case, carrier phase of BDS B1 is used as the benchmark. Figure 4 illustrates the carrier phase biases between BDS B1 and other frequencies (BDS B2, B3, and Galileo E1, E6, E5b), respectively. The biases for BDS B2 and B3 (depicted in blue) remain stable throughout this experiment, with negligible changes in their mean values. The centimeter-level sinusoidal fluctuations indicate significant errors caused by non-negligible multipath effects. For biases between different constellations (BDS B1 and Galileo E1, E6, E5a, shown in orange), they

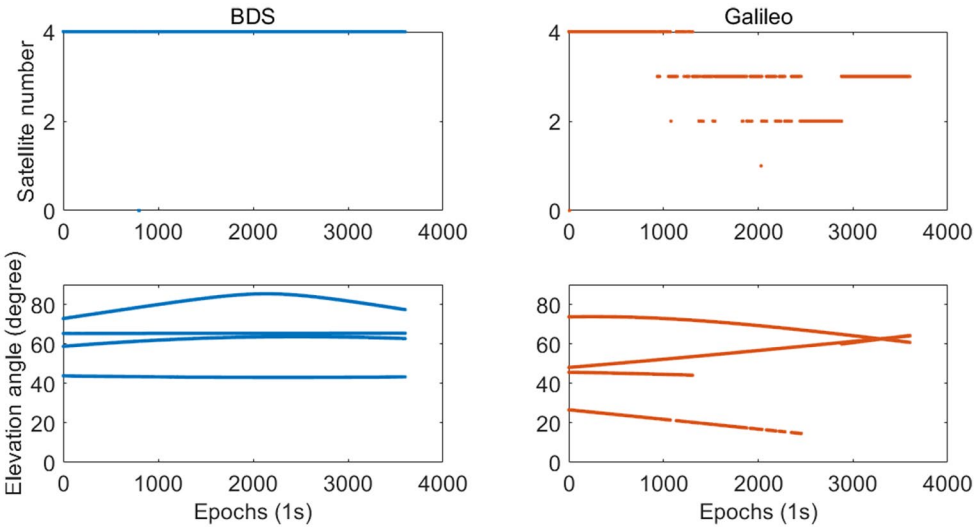

Fig. 3 The number (top) and elevation angle (botton) of visiable satellites from BDS and Galileo in the static experiment

Table 1 The details of the experimental setting in the static experiment

Reference station				Antenna: TRM 59800.00; Receiver: Trimble NetR9	
Rover station				Antenna: Leica AS10; Receiver: SEPT POLARX5E	
Baseline				3.9 km	
Sampling duration				1 h	
Sampling rate				1 Hz	
Constellation	*f1* (MHz)	*f2* (MHz)	*f3* (MHz)	EWL	WL
BDS 2	1561.098	1207.14	1268.52	$\lambda_{(0,-1,1)}$:4.88 m	$\lambda_{(1,-1,0)}$: 0.85 m
Galileo	1575.42	1278.75	1207.14	$\lambda_{(0,1,-1)}$:4.19 m	$\lambda_{(1,-1,0)}$: 1.01 m

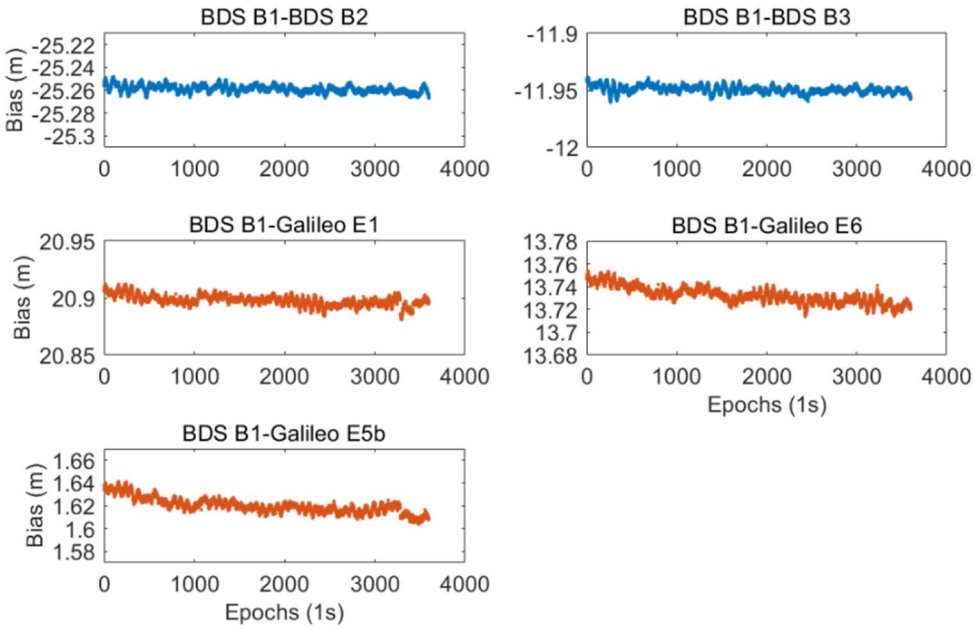

Fig. 4 Biases of other cairrier phases (BDS B2 B3, Galileo E1 E6 E5b) relative to carrier phase in BDS B1 in the static experiment (cycle slips were detected and repaired)

are relatively stable, though not as consistent as those within the same constellation. This discrepancy arises because bias estimation for measurements from different constellations require the antenna position, and errors in antenna positioning reduce the accuracy of the estimated biases. Additionally, residual atmospheric errors further diminish this accuracy.

Theoretically, these biases should be estimated in open-sky areas using an ultra-short baseline (several meters) or a common antenna, where estimations can achieve

Table 2 Bias corrections (m) for all measurements used in the static experiment

Frequency	BDS B1	BDS B2	BDS B3	Galileo E1	Galileo E6	Galileo E5a
Pseudroange	49.96	58.80	64.60	55.99	65.87	59.96
Carrier phase	0	-25.258	-11.949	20.898	13.734	1.621

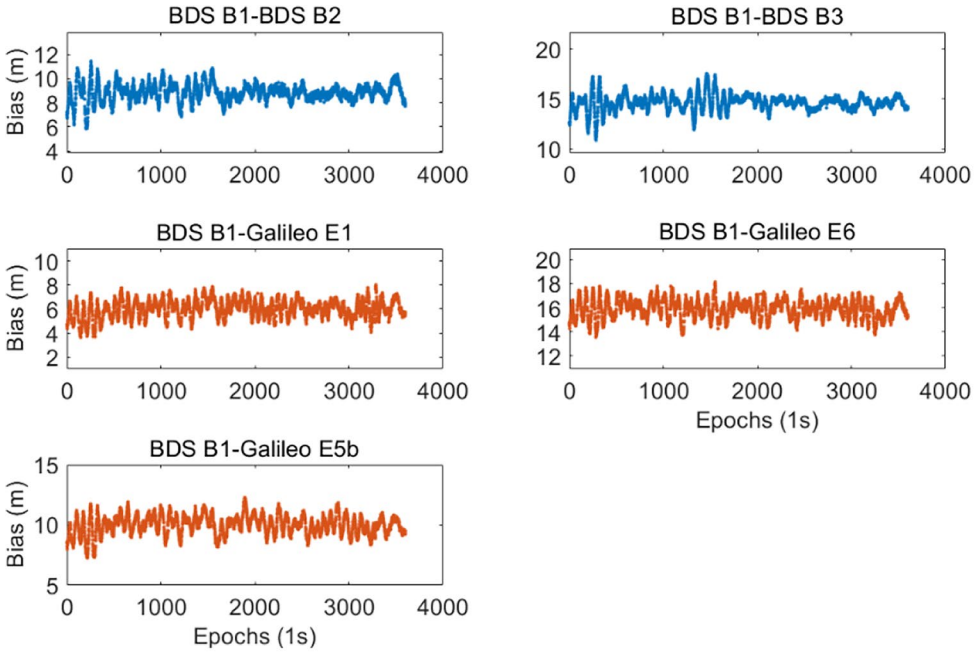

Fig. 5 Biases of other pseudoranges (BDS B2 B3, Galileo E1 E6 E5b) relative to pseudorange in BDS B1 in the static experiment

millimeter-level precision. However, these biases may change when receivers are restarted. Currently, these biases can only be estimated in real-time and remain valid until the receiver is powered off. This paper does not delve into the stability of these inter- or intra-system biases, as they have been extensively investigated in existing research (Odijk et al. 2012; Odijk and Teunissen 2013; Paziewski and Wielgosz 2015; Paziewski et al. 2015; Li et al. 2018; Gao et al. 2018; Gao et al. 2018; Tian et al. 2018; Tian et al. 2019; Zhao et al. 2021). We anticipate that in the future, these biases will be directly calibrated within receivers, eliminating the need for user intervention. Consequently, we treat these biases as constants in this paper. The mean values of these biases from the first five minutes are used to correct the carrier phases in the whole experiment, with detailed corrections presented in Table 2.

The estimation of pseudorange biases is relatively easier, as it does not require consideration of cycle slips. The estimated pseudorange biases are illustrated in Fig. 5. Notably, the variances of these biases are significantly larger than those associated with the carrier phase. Multipath errors are more readily identifiable in these biases compared to the carrier phase. This conclusion holds true even for measurements from the satellites with the highest elevation in the two constellations. It can be inferred that the remaining satellites (with lower elevation angles) exhibit larger multipath errors, which can adversely affect ambiguity resolution.

To ensure successful single-difference ambiguity resolution, it is also essential to estimate and correct the relative biases between pseudorange and carrier phase. Given that the clock errors for all measurements have already been corrected to the BDS B1 frequency, only the pseudorange-carrier bias of BDS B1 requires estimation. The results are presented in Fig. 6, where the mean value can be considered as the approximate pseudorange-carrier bias. Detailed pseudorange corrections for all frequencies are also provided in Table 2.

Figure 6 also depicts the pseudorange multipath error for the BDS satellite with the highest elevation angle, as the carrier phase multipath error is considerably smaller than that of the pseudorange. As shown in the bottom left of Fig. 3, the elevation angle of this satellite gradually increases from approximately 70 degrees, reaching a peak of about 85 degrees around epoch 2000, after which it steadily decreases. Correspondingly, Fig. 6 indicates that the pseudorange multipath error decreases continuously until epoch 2000 and then begins to increase slowly. This further demonstrates that multipath errors in measurements at low elevation angles are significantly larger.

Positioning analysis

In real-time period, when measurements from these frequencies are received, they are calibrated using the specified

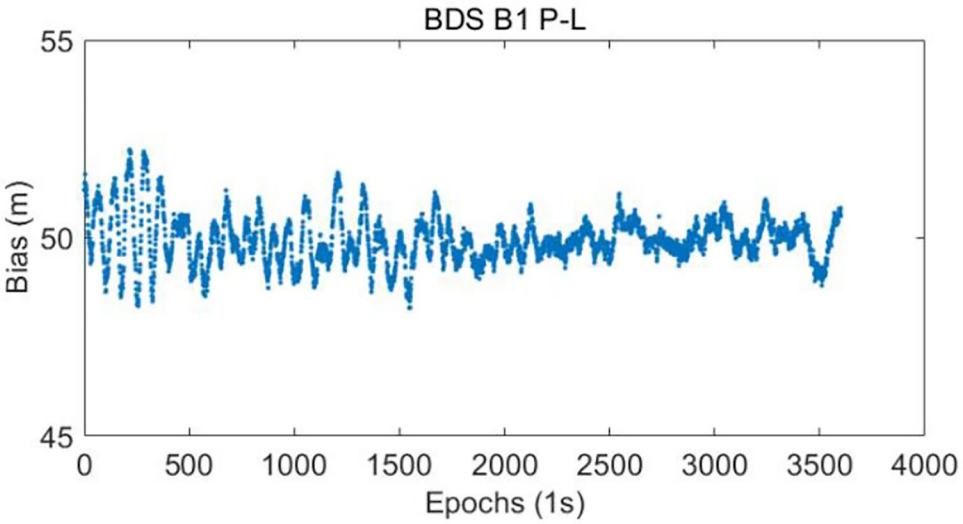

Fig. 6 Bias between pseudorange and carrier phase in BDS B1 in the static experiment

corrections. These corrections remain unchanged until the two receivers are restarted. After the calibration, all measurements exhibit a uniform receiver clock error, allowing for the processing of single-difference ambiguity resolution. Once all ambiguities are resolved, only a mixed receiver clock error needs to be considered during the positioning process, irrespective of the number of constellations involved. This approach enhances the strength of the model when multiple constellations are utilized concurrently. For better comparative analysis, three different algorithms are employed for positioning in this case, and all these algorithms are in single-epoch mode.

1) SD-RANSAC-TCAR (Proposed Algorithm): In this algorithm, the relative biases associated with different measurements are estimated beforehand and subsequently used to calibrate received measurements in real-time. The TCAR is conducted based on between-receiver single-difference measurements. The RANSAC algorithm is employed to detect and exclude satellites with incorrectly resolved ambiguities. Since three positional coordinates and one receiver clock error are unknown, the threshold for inliers is set at five (four unknowns + one redundancy, i.e. 5 satellites) in this case. This implies that positioning is performed when the number of inliers exceeds five.
2) DD-RANSAC-TCAR: Unlike the first approach, this algorithm utilizes intra-system double-difference measurements. The TCAR is then applied to resolve the ambiguity for each satellite-pair. In the RANSAC process, only three positional coordinates are unknown, leading to a threshold of inliers set at four (three unknowns + one redundancy, i.e. $4+n$ satellites), where n represents the number of constellations. It can be find that when more than one constellation is present, the single-difference model requires fewer satellites for positioning ($5<4+n$). Consequently, compared to the intra-system double-difference model, the positional availability of the single-difference model can potentially be enhanced in challenging environments.
3) DD-LAMBDA: Intra-system double-difference measurements are used in the LAMBDA method for ambiguity resolution (Verhagen et al. 2012), and the ratio test is used for ambiguity validation with a threshold 2 (Euler and Schifrin 1991). The presence of non-negligible carrier phase multipath errors diminishes the effectiveness of the ratio test for ambiguity validation in a single-epoch mode. Here we only use this algorithm to show the results under a fixing threshold 2 for comparison.

The positioning results of the three algorithms are presented in Fig. 7. Overall, all results achieve accuracy at centimeter level to decimeter throughout the entire experiment, although with varying levels of availability. The SD-RANSAC-TCAR algorithm demonstrates the highest availability, attributed to its strengthened model. In contrast, the DD-LAMBDA algorithm exhibits the lowest availability, as it lacks fault detection and exclusion mechanisms in its ambiguity resolution process. Among the algorithms depicted in Fig. 7, the DD-RANSAC-TCAR algorithm achieves the highest accuracy, since it only positions when available satellites are more than six (4+2).

For a more comprehensive analysis, the detailed positioning availabilities and the Root Mean Square Error (RMSE) under different numbers of available satellite are summarized in Table 3. Overall, the SD-RANSAC-TCAR algorithm demonstrates the highest positional availability, achieving 3316 epochs, which significantly surpasses the

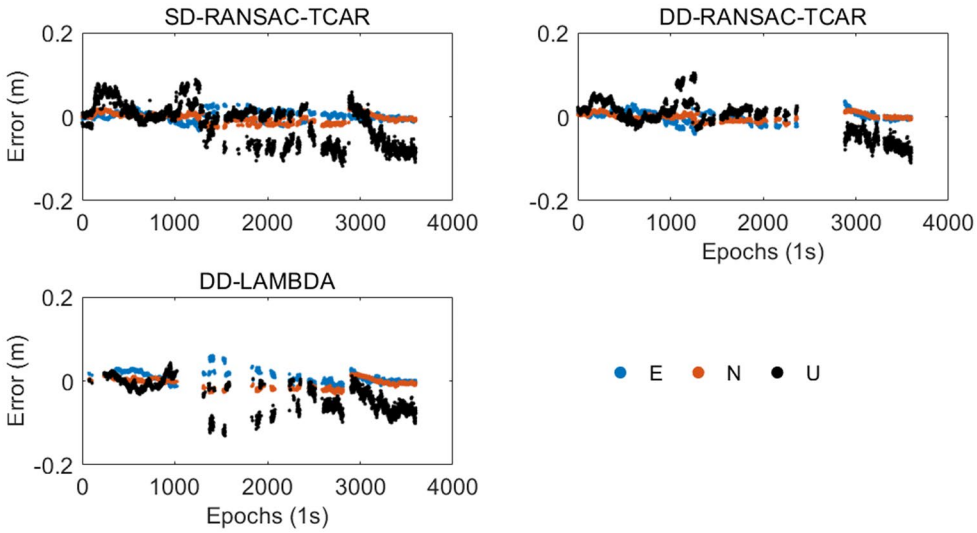

Fig. 7 Positioning errors of static experiment in east north and up directions

Table 3 The 3D RMSE (cm) under different satellite numbers, and the corresponding positional availabilities (epoch)

Satellite number		Less than 6	6	7	8	Total
SD-RANSAC-TCAR	3D RMSE (cm)	NaN	7.48	5.10	3.29	5.03
	Availability (epochs)	0	517	1629	1170	3316
DD-RANSAC-TCAR	3D RMSE (cm)	NaN	NaN	5.12	2.82	4.21
	Availability (epochs)	0	0	1313	1143	2456
DD-LAMBDA	3D RMSE (cm)	NaN	7.89	5.52	2.41	5.43
	Availability (epochs)	0	461	827	673	1961
Total observed epochs		9	702	1719	1170	3600

availabilities of the other two double-difference algorithms, which achieve 2456 and 1961 epochs, respectively.

The positioning accuracy of the three algorithms is comparable, with SD-RANSAC-TCAR achieving an RMSE of 5.03 cm, DD-RANSAC-TCAR at 4.21 cm, and DD-LAMBDA at 5.43 cm. These slight differences can be attributed to the varying percentages of results with different numbers of satellites. An obvious finding from Table 3 is that as the number of satellites increases, the positioning accuracy of the three algorithms improves. When fewer than six satellites are available, none of the algorithms can achieve high-precision positioning. With six visible satellites, SD-RANSAC-TCAR and DD-LAMBDA achieve positional availability at 517 and 461 epochs, respectively, with similar RMSE values of 7.48 cm and 7.89 cm. DD-RANSAC-TCAR is unable to position in this scenario, as it requires more than six satellites, as previously mentioned. This highlights the significance of the proposed single-difference ambiguity resolution, particularly when multiple constellations are utilized. When seven or eight satellites are available, all three algorithms can successfully position. SD-RANSAC-TCAR continues to exhibit the highest availability, with 1629 and 1170 epochs, respectively. It is noteworthy that all epochs tracking eight satellites achieved high-precision positioning with the proposed algorithm. The results of DD-RANSAC-TCAR become more comparable to those of SD-RANSAC-TCAR as the number of satellites increases, achieving 1313 and 1143 epochs for seven and eight satellites, respectively. The fixing rates of DD-LAMBDA decrease as the number of satellites increases. One reason for this is that as the number of satellites increases, the probability of large errors also increases. However, the LAMBDA method lacks an effective mechanism to detect and exclude these satellites. Additionally, a larger number of satellites make it difficult for the searched ambiguities to pass the ratio test. Effectively validating the searched ambiguities using LAMBDA still remains a challenge.

Dynamic field experiment

A vehicular experiment was conducted in urban areas (Nanjing) to further validate the effectiveness of the proposed single-difference TCAR algorithm. The experimental setup is detailed in Table 4. Multiple constellations, including GPS, BDS (2 and 3), Galileo, and the Quasi-Zenith Satellite System (QZSS), were used in this eperiment. The reference trajectory was established using a high-grade Inertial Measurement Unit (IMU), the Honeywell HGuide N580, tightly integrated with GNSS data using software Inertial Explorer (IE) in forward-backward RTK mode. Figure 8 illustrates

Table 4 The details of the experimental setting in vehicular experiment

Reference station			Antenna: Zhongyu HZZACF-S808; Receiver: Trimble BD990		
Rover station			Antenna: Zhongyu ZYACF-S806; Receiver: Trimble BD990		
Baseline			< 7 km		
Sampling duration			About 1 h		
Sampling rate			1 Hz		
Constellation	*f1* (MHz)	*f2* (MHz)	*f3* (MHz)	EWL	WL
GPS	1575.42	1227.60	1176.45	$\lambda_{(0,1,-1)}$:5.86 m	$\lambda_{(1,-1,0)}$: 0.86 m
BDS2	1561.098	1207.14	1268.52	$\lambda_{(0,-1,1)}$:4.88 m	$\lambda_{(1,-1,0)}$: 0.85 m
BDS3	1561.098	1176.45	1268.52	$\lambda_{(0,-1,1)}$:3.26 m	$\lambda_{(1,-1,0)}$: 0.78 m
Galileo	1575.42	1207.14	1176.45	$\lambda_{(0,1,-1)}$:9.77 m	$\lambda_{(1,-1,0)}$: 0.81 m
QZSS	1575.42	1227.60	1176.45	$\lambda_{(0,1,-1)}$:5.86 m	$\lambda_{(1,-1,0)}$: 0.86 m

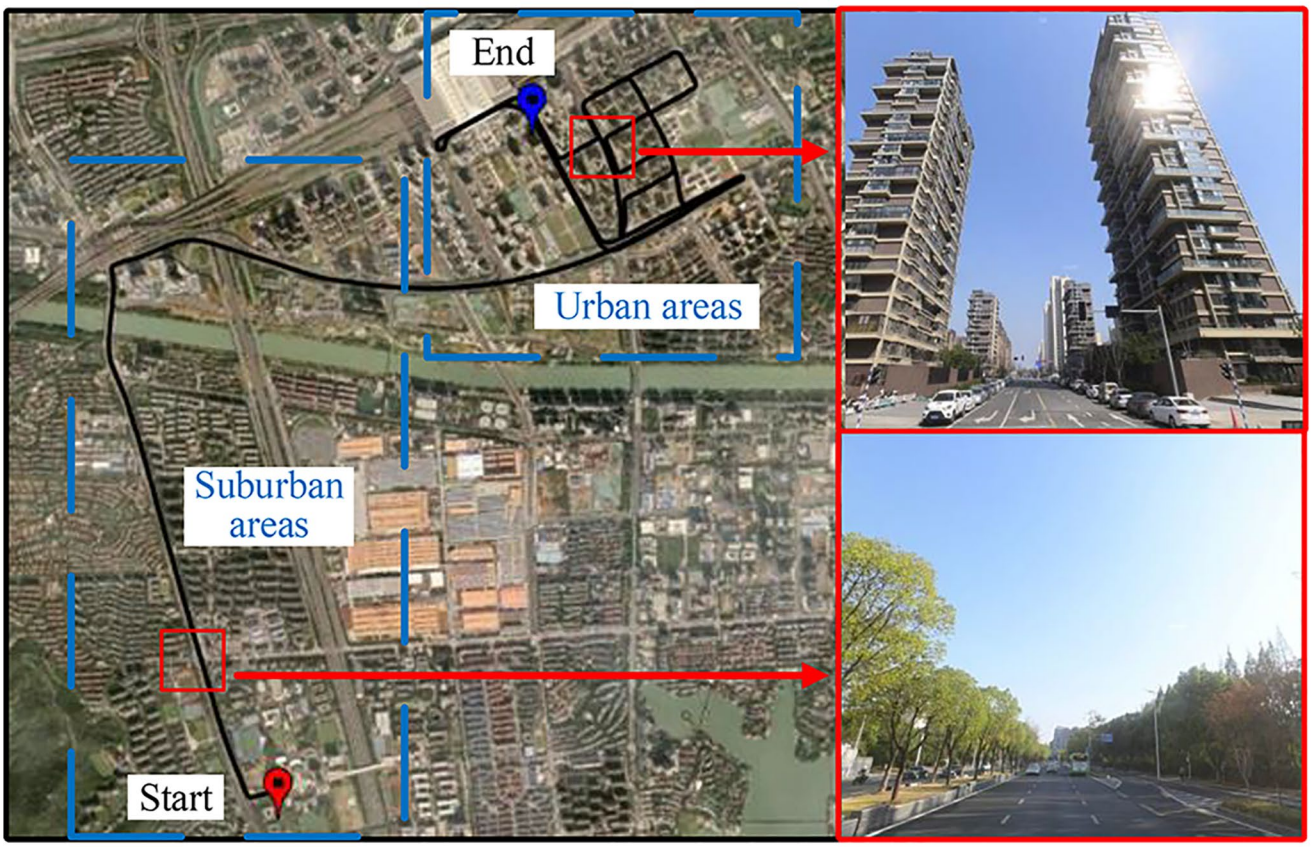

Fig. 8 Vehicular experimental trajectory and environments

the trajectory and the experimental environments. The entire trajectory encompasses both suburban and urban areas.

Biases Estimation

Five-minute data from suburban areas were used for measurement biases estimation. During this estimation period, traditional intra-system double-difference RTK was used for positioning. The fixed solutions were then used to estimate these biases, with GPS L1 as the benchmark.

Positioning analysis

1000s (1 Hz) data from the urban areas in Fig. 8 were used for positioning analysis. The detailed numbers of tracked satellites from different constellations are shown in Fig. 9, and the corresponding three-frequency pseudorange errors of these satellites are shown in Fig. 10, with the maximum up to about 70 m. This indicates that the data quality during this period is poor, which may disable ambiguity resolution.

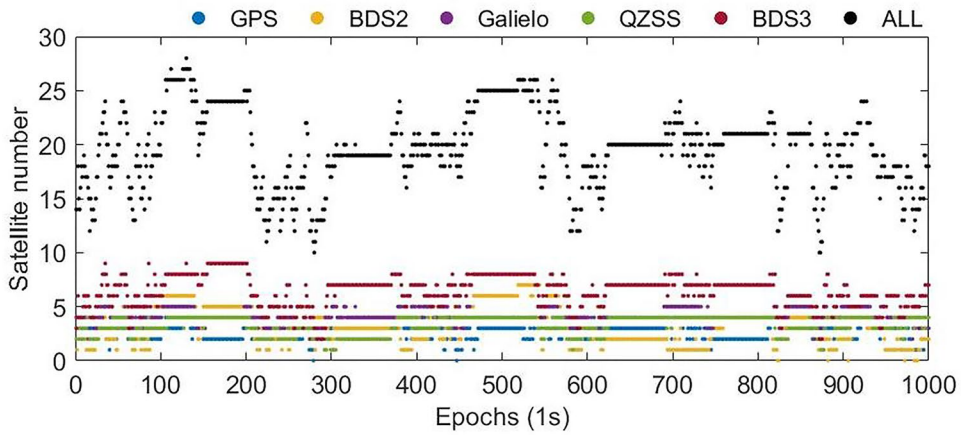

Fig. 9 The number of tracking satellites from different constellations

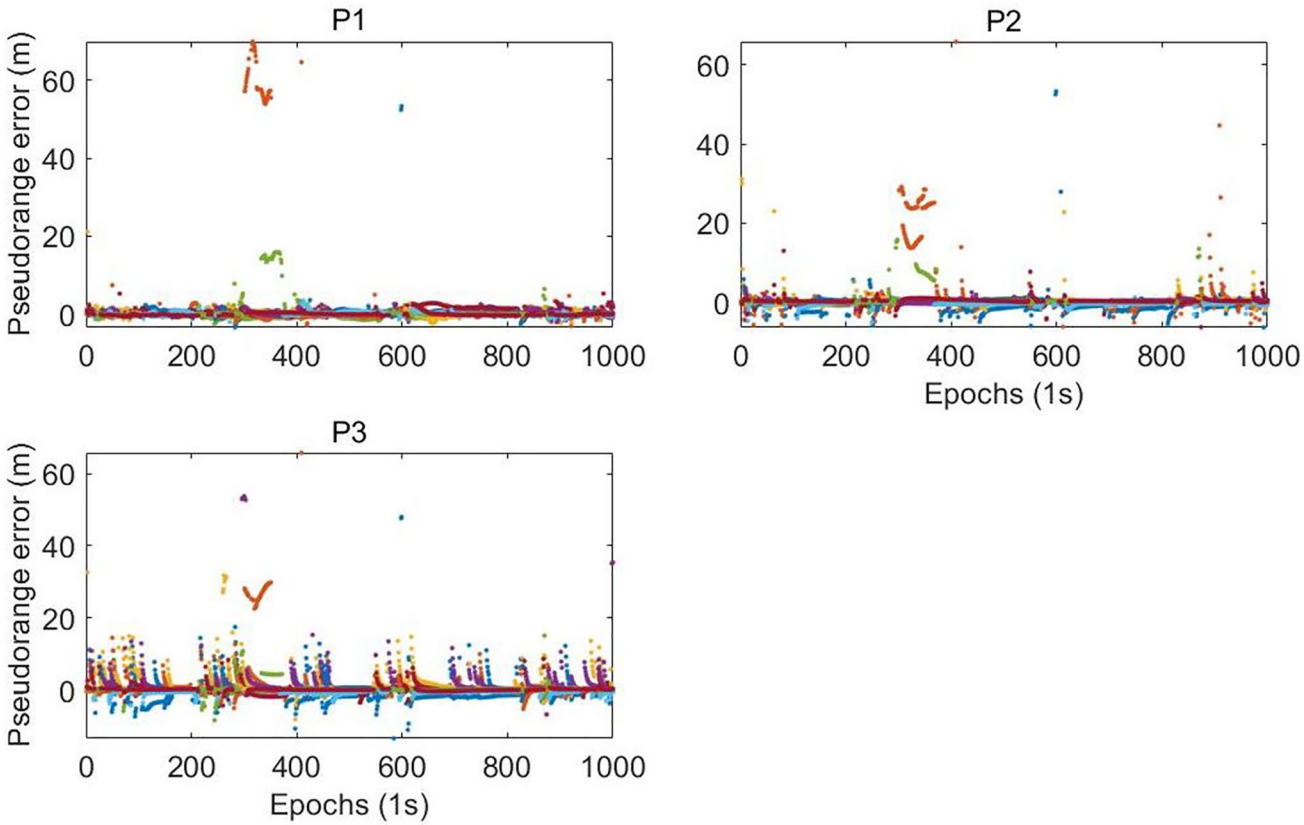

Fig. 10 Double-difference pseudorange errors of all tracking satellites

Similarly, three algorithms are used here for comparison in single-epoch mode.

1) SD-RANSAC-TCAR (Proposed Algorithm): A 15-degree mask angle and a C/N0 threshold 35 dB-Hz were used for initial satellite selection in the vehicular experiment. The threshold for inliers is set at seven (four unknowns + three redundancies, i.e. 7 satellites), due to larger noise. The estimated measurement biases in suburban areas are used here for urban area measurement corrections.
2) DD-RANSAC-TCAR: A 15-degree mask angle and a C/N0 threshold 35 dB-Hz were used for initial satellite selection in the vehicular experiment. The threshold for inliers is set at six (three unknowns + three redundancies, i.e. $6+n$ satellites), where n represents the number of constellations. Other settings are same as that in static experiment.

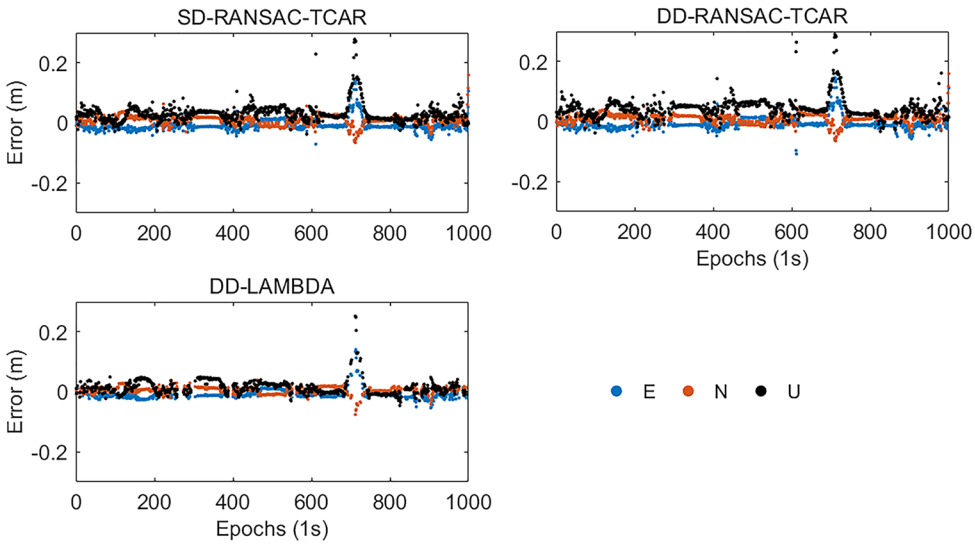

Fig. 11 Positioning errors of vehicular experiment in east north and up directions

Table 5 The 3D RMSE (cm) and the positional availabilities (epoch)

SD-RANSAC-TCAR	3D RMSE (cm)	5.28
	Availability (epochs)	998
DD-RANSAC-TCAR	3D RMSE (cm)	6.33
	Availability (epochs)	947
DD-LAMBDA	3D RMSE (cm)	3.64
	Availability (epochs)	782
Total observed epochs		1000

3) DD-LAMBDA: Since the measurements in the dynamic experiment are very poor, the LAMBDA can fix only a few epochs, with 15-degree mask angle and 35 dB-Hz C/N0 threshold. They are set as 20 degrees and 40 dB-Hz in this case. The threshold is still 2 for the ratio test.

The positioning results of the three algorithms are presented in Fig. 11; Table 5. All three algorithms achieve centimeter-level accuracy, with 3D RMSEs of 5.28 cm, 6.33 cm, and 3.64 cm for the proposed SD-RANSAC-TCAR, DD-RANSAC-TCAR and DD-LAMBDA, respectively. A significant finding is that the proposed algorithm achieves 99.8% positional availability, surpassing the two comparative algorithms. This highlights the great potential of the proposed algorithm to provide high-precision positioning services in challenging environments. Further validation is provided in Fig. 12, which illustrates the fixed solutions of the three algorithms on a map. The GNSS data were collected from typical urban areas with high-rise buildings. The DD-LAMBDA algorithm is sensitive to large GNSS measurement errors, resulting in an inability to fix ambiguities near tall buildings, particularly those with glass facades. Although the fix rate for DD-LAMBDA is 78.2%, nearly half of these fixes occur while waiting at traffic lights at intersections, where the environment is relatively open. This explains why the red portion (not fixed epochs) of DD-LAMBDA in Fig. 12 appears more than 21.8%. The DD-RANSAC-TCAR algorithm can detect and exclude faulty satellites, performing significantly better than DD-LAMBDA. However, its performance is limited by insufficient satellite visibility when tall buildings flank the street, as seen in the zoomed-in section of Fig. 12. The proposed SD-RANSAC-TCAR method achieves an impressive nearly 100% fixed solution rate, demonstrating its superior positioning performance in harsh environments.

Conclusion

The traditional intra-system double-difference model necessitates sacrificing one reference satellite per constellation, which can lead to insufficient satellite-pairs for ambiguity resolution in challenging environments. To address this limitation, we propose a single-difference TCAR algorithm. This algorithm estimates relative measurement biases in advance, which are then used to correct real-time measurements. These biases do not require re-estimation unless there is a significant change in the receiver's internal biases, typically caused by a receiver restart. This approach is superior to the latest inter-system double-difference model, where biases should be re-estimated following a cycle slip in the reference satellite or a change in the reference satellite. The model strength is also further enhanced using the between-receiver single-difference model by calibrating the pseudorange-carrier and multi-frequency (within a constellation) biases, which are ignored in the inter-system double-difference model. The corrected measurements enable instantaneous single-difference TCAR. Additionally, RANSAC is employed to detect and exclude satellites with incorrectly fixed ambiguities before positioning.

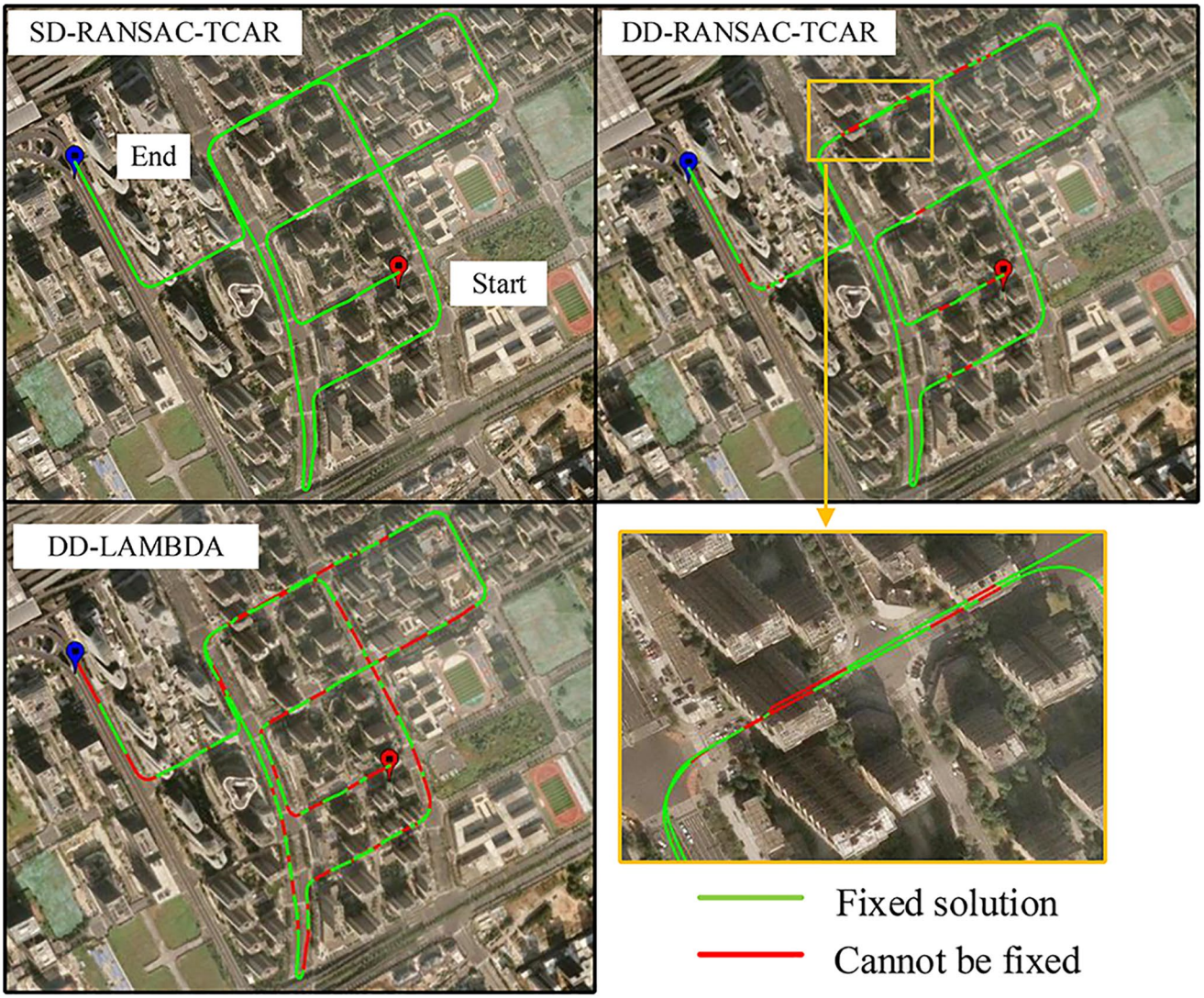

Fig. 12 High-precision positional availabilities (fixed solution) of three algorithms

We conducted both static and vehicular experiments in challenging urban environments to validate the proposed method. In the static experiment, the results demonstrate that the proposed SD-RANSAC-TCAR significantly outperforms DD-RANSAC-TCAR and DD-LAMBDA in terms of positional availability, achieving 92.1% compared to 68.3% and 54.5%, respectively. The positioning accuracies of the three algorithms are comparable, with 3D RMSEs of 5.03 cm (SD-RANSAC-TCAR), 4.41 cm (DD-RANSAC-TCAR), and 5.43 cm (DD-LAMBDA). In the vehicular experiment, GNSS data from suburban areas were used to estimate measurement biases in advance, allowing for real-time correction of new GNSS data. The SD-RANSAC-TCAR achieved nearly 100% positional availability in typical urban areas, with an RMSE of 5.28 cm, outperforming DD-RANSAC-TCAR (94.7% availability, 6.33 cm RMSE) and DD-LAMBDA (78.2% availability, 3.64 cm RMSE). Given that the proposed algorithm can operate in a single-epoch mode once relative measurement biases are estimated, it shows great potential for real-time positioning in challenging environments.

Although the effectiveness of the proposed algorithm has been demonstrated through several experiments, the requirement for prior estimation of these biases remains a limitation. In particularly GNSS challenging environents where these biases cannot be estimated in real time or in advance, the proposed algorithm becomes inapplicable. Nevertheless, there are scenarios in which these biases can be neglected. Many studies have reported that when the same type of receiver (some brands) is used at both the reference and rover stations, these biases become negligible (Håkansson et al. 2017). We believe that with the advancement of receiver technology, these receiver-related biases can be thoroughly addressed in the near future, enabling

receivers to directly output clean data without measurement biases. At that point, the single-difference TCAR method proposed in this paper has the potential to provide high-precision positioning services and demonstrate significant value in challenging urban environments.

Acknowledgements The authors are grateful for the sponsorship of the Hong Kong General Research Fund (Grant No. 15229622), Guangdong - Hong Kong Technology Cooperation Funding Scheme (Grant No. GHP/033/22SZ), the University Grants Committee of Hong Kong under the scheme Research Impact Fund (Grant No. R5009–21) and National Natural Science Foundation of China (Grant No. 42222401, 421740254, 42404052).

Author contributions Q. C. wrote the main manuscript. All authors reviewed the manuscript.

Data availability No datasets were generated or analysed during the current study.

Declarations

Competing interests The authors declare no competing interests.

References

Chen H, Jiang W, Li J (2019) Multi-GNSS relative positioning with fixed inter-system ambiguity. Remote Sens 11(4):454

Chen GE, Li B, Zhang Z, Liu T (2022) Integer ambiguity resolution and precise positioning for tight integration of BDS-3, GPS, GALILEO, and QZSS overlapping frequencies signals. GPS Solut 26:1–16

Cheng Q, Chen W, Sun R, Ding M (2023) Strategy for single-epoch RTK positioning using dual-frequency in urban areas. IEEE Internet of Things Journal

Cheng Q, Chen W, Sun R, Wang J, Weng D (2024) RANSAC-based instantaneous real-time kinematic positioning with GNSS triple-frequency signals in urban areas. J Geodesy 98(4):24

Daneshmand S, Broumandan A, Sokhandan N, Lachapelle G (2013) GNSS multipath mitigation with a moving antenna array. IEEE Trans Aerosp Electron Syst 49(1):693–698

Dyukov A (2016) Mask angle effects on GNSS speed validity in multipath and tree foliage environments. Asian J Appl Sci 4(2):309–321

Euler H, Schaffrin B (1991) On a measure for the discernibility between different ambiguity solutions in the static-kinematic GPS mode. In: kinematic systems in geodesy, surveying, and remote sensing: symposium No. 107 Banff, Alberta, Canada, 10–13 September, 1990 pp 285–295

Fischler MA, Bolles RC (1981) Random sample consensus: a paradigm for model fitting with applications to image analysis and automated cartography. Communications of the ACM 24(6):381–395

Gao W, Meng X, Gao C, Pan S, Wang D (2018) Combined GPS and BDS for single-frequency continuous RTK positioning through real-time Estimation of differential inter-system biases. GPS Solut 22:1–13

Gao W, Pan S, Liu L, Wen H (2021) Tightly combined triple-frequency GPS and BDS for rapid wide-lane RTK positioning with consideration of carrier-phase differential inter-system bias. Int J Distrib Sens Netw 17(3):15501477211003767

Geng J, Li X, Zhao Q, Li G (2019) Inter-system PPP ambiguity resolution between GPS and BeiDou for rapid initialization. J Geodesy 93(3):383–398

Groves PD, Jiang Z (2013) Height aiding, C/N0 weighting and consistency checking for GNSS NLOS and multipath mitigationn in urban areas. J Navig 66(5):653–669

Håkansson M, Jensen AB, Horemuz M, Hedling G (2017) Review of code and phase biases in multi-GNSS positioning. GPS Solut 21:849–860

Heng L, Walter T, Enge P, Gao GX (2014) GNSS multipath and jamming mitigation using high-mask-angle antennas and multiple constellations. IEEE Trans Intell Transp Syst 16(2):741–750

Jiang Z, Groves PD (2014) NLOS GPS signal detection using a dual-polarisation antenna. GPS Solut 18:15–26

Li G, Geng J, Guo J, Zhou S, Lin S (2018) GPS + Galileo tightly combined RTK positioning for medium-to-long baselines based on partial ambiguity resolution. J Glob Position Syst 16(1):3

Li W, Zhu S, Ming Z (2021a) Estimation of Inter-System biases between BDS-3/GPS/Galileo and its application in RTK positioning. Remote Sens 13(17):3507

Li X, Li X, Huang J, Shen Z, Wang B, Yuan Y, Zhang K (2021b) Improving PPP–RTK in urban environment by tightly coupled integration of GNSS and INS. J Geodesy 95:1–18

Li X, Wang S, Li S, Zhou Y, Xia C, Shen Z (2023) Enhancing RTK performance in urban environments by tightly integrating INS and lidar. IEEE Trans Veh Technol 72(8):9845–9856

Malicorne M, Macabiau C, Calmettes V, Bousquet M (2002) Effects of masking angle and multipath on Galileo performances in different environments. In INS 2001, 8th saint petersburg conference on integrated navigation systems 36(1):96

Mi X, Zhang B, Yuan Y (2021) Multi-GNSS RTK positioning with integer ambiguity resolution: from double-differenced to single-differenced. J Global Position Syst 17(2):151–163

Ng HF, Hsu LT (2021) 3D mapping database-aided GNSS RTK and its assessments in urban canyons. IEEE Trans Aerosp Electron Syst 57(5):3150–3166

Odijk D, Teunissen PJG (2013) Estimation of differential inter-system biases between the overlapping frequencies of GPS, Galileo, BeiDou and QZSS. In: Proceedings of 4th international colloquium scientific and fundamental aspects of the Galileo program. Dec 4–6, Prague, Czech Republic

Odijk D, Teunissen PJG, Huisman L (2012) First results of mixed GPS + GIOVE single-frequency RTK in Australia. J Spat Sci 57:3–18

Paziewski J, Wielgosz P (2015) Accounting for Galileo-GPS intersystem biases in precise satellite positioning. J Geod 89(1):81–93

Paziewski J, Sieradzki R, Wielgosz P (2015) Selected properties of GPS and Galileo-IOV receiver intersystem biases in multi-GNSS data processing. Meas Sci Technol 9(26):95008

Shang R, Gao C, Gao W, Zhang R, Peng Z (2020) A single difference-based multi-GNSS inter-system model with consideration of inter-frequency bias and inter-system bias. Meas Sci Technol 32(3):035013

Sun R, Fu L, Wang G, Cheng Q, Hsu LT, Ochieng WY (2021) Using dual-polarization GPS antenna with optimized adaptive neuro-fuzzy inference system to improve single point positioning accuracy in urban canyons. Navigation 68(1):41–60

Tian Y, Liu Z, Ge M, Neitzel F (2018) Determining inter-system bias of GNSS signals with narrowly spaced frequencies for GNSS positioning. J Geodesy 92:873–887

Tian Y, Liu Z, Ge M, Neitzel F (2019) Multi-dimensional particle filter-based Estimation of inter-system phase biases for multi-GNSS real-time integer ambiguity resolution. J Geodesy 93:1073–1087

Tranquilla JM, Carr JP, Al-Rizzo HM (1994) Analysis of a choke ring groundplane for multipath control in global positioning system (GPS) applications. IEEE Trans Antennas Propag 42(7):905–911

Vagle N, Broumandan A, Jafarnia-Jahromi A, Lachapelle G (2016) Performance analysis of GNSS multipath mitigation using antenna arrays. J Global Position Syst 14(1):1–15

Van Dierendonck AJ, Fenton P, Ford T (1992) Theory and performance of narrow correlator spacing in a GPS receiver. Navigation 39(3):265–283

Van Nee RD, Siereveld J, Fenton PC, Townsend BR (1994) The multipath estimating delay lock loop: approaching theoretical accuracy limits. In Proceedings of 1994 IEEE Position, Location and Navigation Symposium-PLANS'94 pp. 246–251

Verhagen S, Li B, Geodesy M (2012) LAMBDA software package: matlab implementation, version 3.0. Delft University of Technology and Curtin University, Perth, Australia

Yang G, Wang Q, Yang Y, Zhou S (2020) A multi-system tightly-combined model with consideration of differential inter-systems code biases. Adv Space Res 66(8):1887–1901

Zhao W, Liu G, Wang S, Gao M, Lv D (2021) Real-time Estimation of GPS-BDS inter-system biases: an improved particle swarm optimization algorithm. Remote Sens 13(16):3214

Zhao W, Liu G, Gao M, Zhang B, Hu S, Lyu M (2023) A new inter-system double-difference RTK model applicable to both overlapping and non-overlapping signal frequencies. Satell Navig 4(1):22